A three-dimensional hybrid finite element/spectral analysis of noise radiation from turbofan inlets

M.C. Duta*, M.B. Giles

Computing Laboratory, University of Oxford, Oxford OX1 3QD, UK

Abstract

This paper describes a new three-dimensional (3D) analysis of tonal noise radiated from non-axisymmetric turbofan inlets. The novelty of the method is in combining a standard finite element discretisation of the acoustic field in the axial and radial coordinates with a Fourier spectral representation in the circumferential direction. The boundary conditions at the farfield, fan face and acoustic liners are treated using the same spectral representation. The resulting set of discrete acoustic equations are solved employing the well-established BICGSTAB or QMR iterative algorithms and a very effective specialised preconditioner based on the axisymmetric mean geometry and flow field. Numerical examples demonstrate the suitability of the new method to engine configurations with realistic 3D features, such as relatively large degrees of asymmetry and spliced acoustic liners. The examples also illustrate the two advantages of the new method over a traditional 3D finite element approach. The new method requires a significantly smaller number of unknowns as relatively few circumferential Fourier modes in the spectral solution ensure an accurate field representation. Also, due to the effective preconditioner, the spectral linear solver benefits from stable iterations at a high rate of convergence.
© 2006 Elsevier Ltd. All rights reserved.

1. Introduction

Aircraft noise emissions are limited by stringent civil aviation regulations in order to reduce the impact on local communities. As a consequence, noise has become a major concern during the design of modern high-bypass turbofan engines in widespread use in civil aircraft. During takeoff and landing, an important component of the total noise consists of tones generated at the fan either by the rotation of shocks attached to fan blades operating at tip speeds exceeding sonic velocity (''buzz-saw'' noise) and/or by rotor–stator interaction (blade passing frequency noise). These tones propagate towards the far field upstream of the engine inlet as well as downstream through the bypass duct. The ability to model the generation and propagation of tone noise along with the mechanisms through which it can be attenuated (acoustic liners in particular) is therefore of paramount importance and has received the attention of considerable research.

There are two important aspects to consider in aeroacoustic analysis: the representation of the unsteadiness of the acoustic phenomena and the mathematical model for the fluid medium. Regarding the first aspect,

*Corresponding author. Tel.: +44 1865 283524; fax: +44 1865 273839.

E-mail address: Mihai.Duta@comlab.ox.ac.uk (M.C. Duta).

Nomenclature

$a_n^{\pm}$	amplitudes of right/left travelling duct eigenmodes	N_n	finite element shape function
c	gas speed of sound	$p, \hat{p}$	pressure and acoustic pressure
f, g	functions used to compute the steady residual	$\mathbf{r}$	vector of nodal steady residual values
		w	finite element test function
$\hat{f}, \hat{g}$	functions used to compute the linear residual	x, r, θ	cylindrical coordinates
		Z	impedance value of the acoustic liner model
$\hat{\mathbf{F}}$	boundary operator of discrete acoustic linear system	$\beta, \hat{\beta}$	boundary term of steady (and acoustic) weak formulation
$\mathbf{J}$	Jacobian transformation from physical coordinates to the coordinates of the canonical finite element	γ	specific heat ratio of the gas
		κ	circumferential mode number of noise source
$k_n^{\pm}$	axial wavenumbers of right/left travelling duct eigenmodes	ξ, η	coordinates of the canonical finite element
$\mathbf{K}$	Jacobian of discrete mean flow problem	$\rho, \hat{\rho}$	density and acoustic density
$\hat{\mathbf{L}}$	volume operator of discrete acoustic linear system	$\phi, \hat{\phi}$	steady (mean) and linear (acoustic) flow potential functions
m, M	circumferential mode number and maximal value in the spectral representation $(-M \leqslant m \leqslant +M)$	$\mathbf{\Phi}$	vector of nodal steady potential values
		$\hat{\mathbf{\Phi}}$	vector of nodal linear potential values
Ma	Mach number	ω	frequency of noise source
$\mathbf{n}$	boundary normal	∞	subscript to denote freestream gas conditions
		0	subscript to denote axisymmetric analysis quantities

numerical methods for the prediction of engine inlet tone noise propagation follow either the time-domain or the frequency-domain approach. In recent years, time-domain methods [1,2] have become more attractive with low cost computing power and have the advantage of being able to model directly multi-frequency sources and acoustic field nonlinearities. However, these methods have an important drawback in the treatment of the frequency-dependent acoustic lining material and, despite recent efforts [3,4], direct modelling of the acoustic response of the lining in the time-domain will continue to be relatively expensive. By contrast, frequency-domain methods [5,6] are much faster than their time-domain counterparts and treat acoustic liners in a natural way by modelling their acoustic response at given frequencies. Methods in this class will probably continue to be developed and used in the foreseeable future.

The other important aspect of aeroacoustic analysis is the fluid model which can range from the velocity potential equation [7,8] to the full Navier–Stokes [9,10]. Whereas modelling nonlinear wave interactions using the Euler or Navier–Stokes equations is particularly important for understanding the generation of tone noise, the potential model is perfectly adequate for the propagation of tone noise in the nearfield at the subsonic conditions during takeoff and landing [10].

This paper introduces a novel 3D method for the analysis of tone noise radiated from non-axisymmetric turbofan inlets based on the frequency-domain potential model. The novelty of the method is in combining a standard finite element (FE) discretisation of the acoustic field in the axial and radial coordinates with a Fourier spectral representation in the circumferential direction. The use of pseudo-spectral methods for the solution of partial differential equations is not new and the applications are already very diverse [11]. The Fourier spectral representation is such a method [12] and shares the advantages of the class of pseudo-spectral methods. The advantage most important for predicting noise radiation from engine inlets is the ability to represent mildly non-axisymmetric geometries using a relatively modest number of Fourier modes. Because only a few Fourier modes need be retained for an accurate representation of the acoustic solution in the circumferential coordinate, the new method involves substantially fewer discrete unknowns than a conventional 3D FE analysis and is consequently less computationally costly. In more challenging cases

such as acoustic liners with circumferentially discontinuous properties, the number of Fourier modes necessary to model the acoustic field is greater than in the case of a smooth variation, nevertheless the overall number of discrete unknowns is still substantially smaller than the requirements for the traditional FE analysis.

Two further features contribute to the attractiveness of the new 3D method for engine inlet applications. First, the system of discrete acoustic equations is solved iteratively using the well-established BICGSTAB or QMR algorithms. There is no need to explicitly form the system matrix as these iterative methods need only the residual terms of the discrete equations. This, combined with the small number of discrete unknowns, results in relatively low computer memory requirements for the new method. Second, the convergence of the iterative algorithms is improved enormously using a preconditioner based on the axisymmetric mean of the 3D geometry and flow field.

Finally, numerical examples are provided to demonstrate the suitability of the new method to engine configurations with realistic 3D features, such as relatively large degrees of asymmetry and spliced acoustic liners.

2. Aeroacoustic model

2.1. Governing equations

At the low subsonic Mach number flow conditions during aircraft take-off and landing approach, it is standard to assume air an ideal gas, non-heat conducting and with constant specific heats as well as to treat its flow past the engine inlet as inviscid, isentropic and irrotational. Hence, the unsteady velocity field of the flow is the gradient of a potential function ϕ while the density and speed of sound are given by

$$\left(\frac{\rho}{\rho_\infty}\right)^{\gamma-1} = \left(\frac{c}{c_\infty}\right)^2 = 1 - (\gamma - 1)\frac{q - q_\infty}{c_\infty},$$

with $q = \nabla\phi \cdot \nabla\phi/2 + \partial\phi/\partial t$ and based on the freestream values of density ρ_∞ and speed of sound c_∞. Choosing the non-dimensionalisation $\rho_\infty = 1$ and $c_\infty = 1$, air density is a function of the potential ϕ and freestream Mach number Ma_∞:

$$\rho^{\gamma-1} = 1 + \frac{1}{2}(\gamma - 1)\left(Ma_\infty^2 - \nabla\phi \cdot \nabla\phi - 2\frac{\partial\phi}{\partial t}\right). \tag{1}$$

Propagation of acoustic waves is approximated as an irrotational and isentropic process, modelled as a harmonic perturbation of small amplitude $\hat{\phi}$ and known frequency ω superposed on a steady mean flow ϕ. The unsteady velocity potential field is thus $\phi + \Re\{\hat{\phi}\exp(i\omega t)\}$, with both the steady flow and the acoustic potential functions being unknown.

Firstly, ignoring acoustic phenomena, the external air flow is considered uniform, steady and parallel to the axis of symmetry of the engine. Then, the steady air flow past the inlet is the solution ϕ of the nonlinear equation of mass conservation:

$$\nabla \cdot (\rho \nabla \phi) = 0. \tag{2}$$

Secondly, the amplitude $\hat{\phi}$ of harmonic unsteadiness is the solution to the partial differential equation

$$\nabla \cdot (\rho \nabla \hat{\phi} + \hat{\rho} \nabla \phi) + i\omega\hat{\rho} = 0, \tag{3}$$

the frequency domain linearisation of the unsteady mass conservation equation. Similarly, the amplitude of linear harmonic density variation is the linearisation of Eq. (1), i.e.

$$\hat{\rho} = -\frac{\rho}{c^2}(\nabla\phi \cdot \nabla\hat{\phi} + i\omega\hat{\phi}), \tag{4}$$

where ρ and c are the density and speed of sound of the steady mean flow.

2.2. Weak formulation

The typical computational domain V for engine inlet aeroacoustics is depicted in Fig. 1. The domain boundaries ∂V are the circular fan face, where the noise source is modelled, the solid inlet wall, possibly incorporating acoustic lining, and the far-field boundary where the infinite physical domain is truncated. Additionally, there is an axis of symmetry in the case of a 2D axisymmetric calculation.

The new aeroacoustic method introduced in this paper is based on the weak formulation of Eqs. (2) and (3), obtained through partial integration over the computational domain V. Thus, mass conservation in weak formulation is

$$\int_V \rho \nabla \phi \cdot \nabla w \, dV - \int_{\partial V} \beta w \, dS = 0, \tag{5}$$

holding for all test functions w in the Sobolev space H_0^1 defined on V. The boundary integral involves the boundary mass flux $\beta = \rho \nabla \phi \cdot \mathbf{n}$, with $\mathbf{n}$ being the outward pointing boundary normal.

Likewise, the weak formulation of the acoustic equation is

$$\int_V \rho \nabla \hat{\phi} \cdot \nabla w - \frac{\rho}{c^2} (\nabla \phi \cdot \nabla \hat{\phi} + i\omega\hat{\phi})(\nabla \phi \cdot \nabla w - i\omega w) \, dV - \int_{\partial V} \hat{\beta} w \, dS = 0, \tag{6}$$

in which the boundary parameter represents the harmonic component of the normal mass flux:

$$\hat{\beta} = \rho \nabla \hat{\phi} \cdot \mathbf{n} - \frac{\rho}{c^2} (\nabla \phi \cdot \nabla \hat{\phi} + i\omega\hat{\phi}) \nabla \phi \cdot \mathbf{n}. \tag{7}$$

2.3. Boundary conditions

The steady mean flow problem has a Dirichlet boundary condition on the far-field boundary to match the uniform freestream condition as well as Neumann boundary conditions $\beta = 0$ on the inlet wall and β prescribed a non-zero value on the fan face boundary to give the required steady mass flow through the engine.

All boundary conditions for inlet aeroacoustics are represented through the parameter $\hat{\beta}$. First, at the farfield, ray theory is used to determine the angle at which the acoustic waves cross the boundary and establish an expression for $\hat{\beta}$ which minimises the reflection of acoustic waves back into the computational domain. The far-field boundary can be assumed axially symmetric without loss of generality; let $\mathbf{n} = (n_x, n_r)^T$ denote the boundary normal. At the farfield, the acoustic potential $\hat{\phi}$ has a (relatively) slowly varying amplitude and a fast varying phase, expressed as $\exp(i\varphi(x, r) + i\kappa\theta)$, where κ is the circumferential wavenumber. With this observation, the boundary parameter becomes

$$\hat{\beta} = i((1 - Ma_\infty^2)n_x k_x + n_r k_r - Ma_\infty \omega n_x)\hat{\phi}, \tag{8}$$
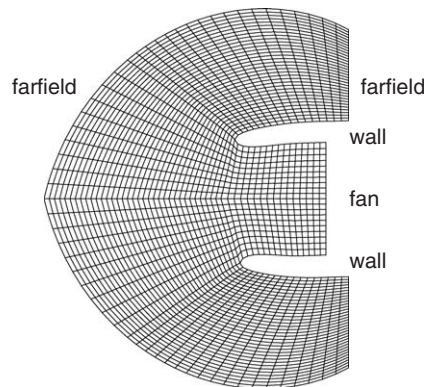

Fig. 1. Vertical axial section through a 3D computational domain and mesh around an asymmetric engine inlet geometry showing the boundaries at the fan face, inlet wall and farfield. (The mesh shown is much coarser than that required by a realistic aeroacoustic calculation.)

where $k_x = \partial\varphi/\partial x$ and $k_r = \partial\varphi/\partial r$ denote the local wavenumbers. Also, introducing the same fast varying phase expression of $\hat{\phi}$ into Eq. (3), a high-frequency WKB analysis gives the dispersion relation:

$$(Ma_\infty k_x + \omega)^2 = k_x^2 + k_r^2 + \frac{\kappa^2}{r^2}.$$

Acoustic waves of high frequency and high circumferential wavenumber radiate toward the farfield from a narrow annular region close to the inlet highlight and, in ray theory approximation, travel along straight lines. Therefore, the angle at which waves arrive at any point on the far-field boundary is given by the unit vector $(e_x, e_r)^T$ from the inlet highlight to that point. Equating the group velocity $(\partial\omega/\partial k_x, \partial\omega/\partial k_r)$ associated with the dispersion relation to the geometric term $\lambda(e_x, e_r)^T/(Ma_\infty k_x + \omega)$ and substituting in the dispersion relation, the following quadratic equation results:

$$(e_x^2 + (1 - Ma_\infty^2)e_r^2)\lambda^2 = \omega^2 - (1 - Ma_\infty^2)\frac{\kappa^2}{r^2}.$$

A positive real root is sought, corresponding to the propagation of acoustic energy from the inlet to the farfield. With this root, the local wavenumbers are given by

$$k_x = -\frac{\lambda e_x - \omega Ma_\infty}{1 - Ma_\infty^2}, \quad k_r = -\lambda e_r$$

and substitution into Eq. (8) yields

$$\hat{\beta} = -\mathrm{i}\rho\lambda(n_x e_x + n_r e_r)\hat{\phi}. \tag{9}$$

For small radii r for which the roots are imaginary, corresponding to the impossibility of local propagation of the assumed form, one can take $\lambda = 0$.

There are two cases of the boundary condition at the engine inlet surface. If the surface is solid, the unsteady normal velocity through the boundary surface is zero and the harmonic normal flux is simply $\hat{\beta} = 0$, corresponding to a perfectly reflecting surface. Where an acoustic liner is present, the boundary condition follows the approach of Eversman [13] based on the modelling of Myers [14]. In this approach, the non-zero unsteady normal velocity is related to the acoustic pressure through a linear frequency-domain equation involving the non-dimensional complex-valued liner impedance Z. Physically, a positive real component of Z corresponds to an absorption of acoustic energy by the liner. Using this equation, the boundary integral contribution to the weak formulation of the inlet acoustics becomes

$$\int_{\partial V} \hat{\beta} w \, \mathrm{d}S = \int_{\partial V} \frac{\mathrm{i}}{\omega Z}\frac{\rho}{c}(\nabla\phi \cdot \nabla\hat{\phi} + \mathrm{i}\omega\hat{\phi})(\nabla\phi \cdot \nabla w - \mathrm{i}\omega w)\,\mathrm{d}S. \tag{10}$$

Because the steady flow is tangential to the surface, this integral involves only tangential derivatives of the unsteady potential $\hat{\phi}$.

Lastly, the condition at the fan boundary is formulated following the modal approach of Astley [7] and Eversman [8]. In this approach, the acoustic field is decomposed into right and left travelling duct eigenmodes and $\hat{\beta}$ becomes a function of the eigenmodes incident at the fan face and models the presence of the downstream fan as the source of noise.

At the fan, the inlet is locally a cylindrical duct of radius R where flow is assumed uniform and isentropic, with Mach number Ma, density ρ and speed of sound c. Then, as the duct eigenmodes have the form $\hat{\phi}(r)\exp(\mathrm{i}kx + \mathrm{i}\kappa\theta + \mathrm{i}\omega t)$, the acoustic propagation equation (6) gives rise to the weak form of the duct acoustics eigenvalue problem

$$\int_0^R \frac{\mathrm{d}\hat{\phi}}{\mathrm{d}r}\frac{\mathrm{d}w}{\mathrm{d}r} + \left(\frac{\kappa^2}{r^2} + k^2 - \left(Ma\,k + \frac{\omega}{c}\right)^2\right)\hat{\phi}wr\,\mathrm{d}r = 0,$$

which holds for any test function w in H_0^1 defined on the interval $[0, R]$. Analytically, the eigenfunction amplitudes $\hat{\phi}$ of this problem are Bessel functions; however, it is more convenient to compute them numerically by performing the eigenmode analysis using a similar finite element discretisation to the main equations. Thus, the eigenvalue problem is first discretised in the radial coordinate and the discrete eigenvalues

$\lambda = (Ma\,k + \omega/c)^2 - k^2$ and eigenfunctions are found. For each value of λ (real and positive), two axial wavenumbers are determined; one wavenumber k^+ corresponds to a right travelling duct mode and the other k^- to a left travelling one. Using these, the harmonic potential at the fan face decomposes as

$$\hat{\phi}(x, r, \theta) = \sum_n (a_n^+\, \mathrm{e}^{\mathrm{i}k_n^+ x} + a_n^-\, \mathrm{e}^{\mathrm{i}k_n^- x})\hat{\phi}_n(r)\, \mathrm{e}^{\mathrm{i}\kappa\theta},$$

in which $\hat{\phi}_n$ are the duct acoustic eigenmodes and $a_n^\pm$ the modal amplitudes. Normally, this decomposition includes all the cut-on modes plus a few above cut-off [15]; however, all cut-off modes are retained in the present analysis along with the cut-on as this leads to a simpler formulation of the discrete acoustic equations.

At the fan face, a_n^- are the amplitudes of the energising incident modes and are known while the amplitudes a_n^+ of the duct modes reflected back from the computational domain have to be found along with the acoustic solution. The fan boundary can be conventionally chosen at $x = 0$ so, due to duct mode orthogonality, the harmonic normal flux through the boundary can be shown to be

$$\hat{\beta} = \sum_n (a_n^+ \sigma_n^+ + a_n^- \sigma_n^-)\hat{\phi}_n(r)\, \mathrm{e}^{\mathrm{i}\kappa\theta}, \tag{11}$$

where

$$\sigma_n^\pm = \mathrm{i}\rho(1 - Ma^2)k_n^\pm - \mathrm{i}\rho Ma\omega/c. \tag{12}$$

Also, using an appropriate normalisation, the following important relationship arises due to orthogonality of the eigenmodes:

$$\int_0^R \hat{\phi}_n(r)\hat{\phi}_n(0, r)r\,\mathrm{d}r = a_n^+ + a_n^-. \tag{13}$$

3. Axisymmetric discretisation

The simple axisymmetric case is considered first, introducing the notation and concepts which are used in the non-axisymmetric analysis discussed in the next section. If the inlet is axisymmetric, the acoustic problem is 2D in the axial x and radial r coordinates. The mesh is composed of quadrilateral elements in the (x, r) axisymmetric coordinates and, following a standard FE approach, each individual element is mapped to a canonical element in the (ξ, η) computational coordinates. The potential field is then represented within each canonical element as an interpolation using the unknown nodal values ϕ_n and the shape functions N_n defined on the canonical element to have the value unity at node n and zero at the other. Using iso-parametric elements, the coordinates are represented in the same manner as the field values and the FE approximation is given by the nodal summations:

$$x(\xi, \eta) = \sum_n x_n N_n(\xi, \eta), \quad r(\xi, \eta) = \sum_n r_n N_n(\xi, \eta), \quad \phi(\xi, \eta) = \sum_n \phi_n N_n(\xi, \eta). \tag{14}$$

Mainly, nine-node bi-quadratic Lagrangian quadrilateral elements were used in this research, however four-node bi-linear elements were also used during the validation of the computer code.

Using the interpolation (14) and the test functions $w = 1/2\pi N_n$, the FE discretisation of the steady mean flow weak formulation (5) yields a set of equations written collectively as

$$\mathbf{r}_0(\boldsymbol{\Phi}_0) = 0. \tag{15}$$

$\boldsymbol{\Phi}_0$ represents the vector of discrete axisymmetric steady potential values ϕ_n associated with the nodes of the mesh and $\mathbf{r}_0$ is the vector of discrete nonlinear residuals. This system of equations is nonlinear in $\boldsymbol{\Phi}_0$ and is solved using a Newton iteration whose update at step k is the solution of

$$\mathbf{K}_0 \Delta\boldsymbol{\Phi}_0^{(k)} = -\mathbf{r}_0\left(\boldsymbol{\Phi}_0^{(k)}\right). \tag{16}$$

The Jacobian matrix $\mathbf{K}_0 = \partial \mathbf{r}_0 / \partial \mathbf{\Phi}_0$ is symmetric and positive definite with its (n, n')th entry given by

$$\mathbf{K}_{0,nn'} = \int_0^1 \int_0^1 \rho \left\{ \nabla N_n \cdot \nabla N_{n'} - \frac{1}{c^2} (\nabla \phi \cdot \nabla N_n)(\nabla \phi \cdot \nabla N_{n'}) \right\} r |J_0| \, \mathrm{d}\xi \, \mathrm{d}\eta, \tag{17}$$

with ρ, c and $\nabla \phi$ evaluated from the current solution iterate $\mathbf{\Phi}^{(k)}$. $\mathbf{J}_0 = \partial(x, r)/\partial(\xi, \eta)$ is the Jacobian of the transformation from the physical coordinates to the computational and the area integral is evaluated through Gauss quadrature on the canonical element. Lastly, the Newton iterations for the axisymmetric mean flow problem are initialised with $\mathbf{\Phi}_0^{(0)} = \mathbf{x}$ ($\mathbf{x}$ is the vector of nodal axial coordinates) and the Newton update is computed from Eq. (16) using a sparse direct linear solver.

The axisymmetric acoustic solution has the general form $\hat{\phi}(x, r) \exp(\mathrm{i}\omega t + \mathrm{i}\kappa \theta)$ in which the circumferential mode number κ is an input to the problem, being defined by the condition at the fan boundary. This suggests the FE approximation

$$\hat{\phi}(\xi, \eta, \theta) = \sum_n \hat{\phi}_n N_n(\xi, \eta) \exp(\mathrm{i}\kappa \theta),$$

which, used with Eq. (14) and the test functions $w = 1/2\pi \exp(-\mathrm{i}\kappa \theta) N_n$, discretises the weak formulation (6) of the acoustic problem to give the linear system of equations:

$$(\hat{\mathbf{L}}_0 + \hat{\mathbf{F}}_0)\hat{\mathbf{\Phi}}_0 = \hat{\mathbf{f}}_0. \tag{18}$$

The unknown $\hat{\mathbf{\Phi}}_0$ is the vector of nodal values $\hat{\phi}_n$ of the linear axisymmetric potential.

The matrix in Eq. (18) is the sum of two linear operators, $\hat{\mathbf{L}}_0$ and $\hat{\mathbf{F}}_0$, which, respectively, come from the discretisation of the volume integral and the boundary surface integral in Eq. (6). The linear harmonic operator $\hat{\mathbf{L}}_0$ has the form

$$\hat{\mathbf{L}}_0 = -\omega^2 \mathbf{M}_0 + \mathrm{i}\omega \mathbf{C}_0 + \mathbf{K}_0 + \kappa^2 \mathbf{K}_\theta. \tag{19}$$

While $\mathbf{K}_0$ has already been described in Eq. (17), the (n, n')th entries of the other matrices are, respectively, defined by

$$\mathbf{M}_{0,n,n'} = \int_0^1 \int_0^1 \frac{\rho}{c^2} N_n N_{n'} r |\mathbf{J}_0| \, \mathrm{d}\xi \, \mathrm{d}\eta, \tag{20}$$

$$\mathbf{C}_{0,n,n'} = \int_0^1 \int_0^1 \frac{\rho}{c^2} \nabla \phi \cdot (N_n \nabla N_{n'} - N_{n'} \nabla N_n) r |\mathbf{J}_0| \, \mathrm{d}\xi \, \mathrm{d}\eta, \tag{21}$$

$$\mathbf{K}_{\theta,n,n'} = \int_0^1 \int_0^1 \rho N_n N_{n'} r^{-1} |\mathbf{J}_0| \, \mathrm{d}\xi \, \mathrm{d}\eta. \tag{22}$$

The boundary operator $\hat{\mathbf{F}}_0$ has three contributions; the first two are the discretisation of the farfield and acoustic liner boundary integrals (9) and (10), respectively. Thus, the (n, n')th entry of the far-field contribution to $\hat{\mathbf{F}}_0$ is

$$-\int_0^1 \int_0^1 \mathrm{i}\rho \lambda (n_x e_x + n_r e_r) N_{n'}^{\mathrm{T}} N_n r |\mathbf{J}_0| \, \mathrm{d}\xi \, \mathrm{d}\eta, \tag{23}$$

while that of the acoustic liner contribution is

$$-\int_0^1 \int_0^1 \frac{\mathrm{i}}{\omega Z} \frac{\rho}{c} (\nabla \phi \cdot \nabla N_{n'} + \mathrm{i}\omega N_{n'})(\nabla \phi \cdot \nabla N_n - \mathrm{i}\omega N_n) r |\mathbf{J}_0| \, \mathrm{d}\xi \, \mathrm{d}\eta. \tag{24}$$

The third contribution to $\hat{\mathbf{F}}_0$ comes from the use of the modal duct boundary conditions at the fan boundary. While the amplitudes a_n^- of the incoming acoustic modes are prescribed by the boundary condition, the amplitudes a_n^+ of the reflected modes are unknown. Following previous work [8,15], the original acoustic equations obtained as the discretisation of Eq. (6) are expanded to include the unknown amplitudes alongside with the linear harmonic potential values by adding the FE discretisation of the duct eigenmode

relationship (13). The extended system of discrete acoustic equations is

$$
\begin{pmatrix} \hat{\mathbf{L}}_0 + \hat{\mathbf{F}}'_0 & -\hat{\mathbf{E}}\Sigma^+ \\ \hat{\mathbf{E}}^{\mathrm{T}} & -I \end{pmatrix} \begin{pmatrix} \hat{\boldsymbol{\Phi}}_0 \\ \mathbf{a}^+ \end{pmatrix} = \begin{pmatrix} \hat{\mathbf{E}}\Sigma^- \mathbf{a}^- \\ \mathbf{a}^- \end{pmatrix},
$$

with $\hat{\mathbf{F}}'_0$ representing the boundary conditions at the farfield and acoustic liner. $\hat{\mathbf{E}}$ is the rectangular matrix of eigenvectors of the discrete duct eigenvalue problem, $\Sigma^{\pm}$ are diagonal matrices with the entries $\sigma^{\pm}$ given by Eq. (12) and $\mathbf{a}^{\pm}$ are the vectors of modal amplitudes in the modal decomposition. Eliminating the unknown amplitudes $\mathbf{a}^+$ from the expanded system, the volume integral operator $\hat{\mathbf{L}}_0$ remains unchanged but the boundary operator has an extra contribution from the fan condition which has the form:

$$
\hat{\mathbf{F}}_0 = \hat{\mathbf{F}}'_0 - \hat{\mathbf{E}}\Sigma^+ \hat{\mathbf{E}}^{\mathrm{T}}. \tag{25}
$$

Also as a result of this, the forcing term of Eq. (18) is revealed to be

$$
\hat{\mathbf{f}}_0 = \hat{\mathbf{E}}(\Sigma^- - \Sigma^+)\mathbf{a}^-, \tag{26}
$$

which reflects the fact that the fan is the only source of acoustic excitation.

Finally, similar to the mean flow Newton update, the algebraic system (18) is solved using a standard direct solution method for sparse systems.

4. Non-axisymmetric discretisation

4.1. Spectral representation

Having discussed the simpler axisymmetric case, the key to the non-axisymmetric solution is to retain the FE approximation in the axial and radial coordinates but to represent the variation of the geometry, mean flow and acoustic field in the circumferential direction using a spectral Fourier series. To illustrate this idea, suppose the starting point for the aeroacoustic analysis is a 3D Computer Aided Design model of an engine inlet. First, the inlet model is "sampled" at a number of θ stations, such that a series of axial sections is obtained, as shown in Fig. 2(a). Then, each axial section of the inlet is discretised using a series of nodes such that each node in one section has a correspondent in the circumferential direction on each other axial section. This can be achieved, for example, by using a curvilinear coordinate varying from 0 to 1 along each section
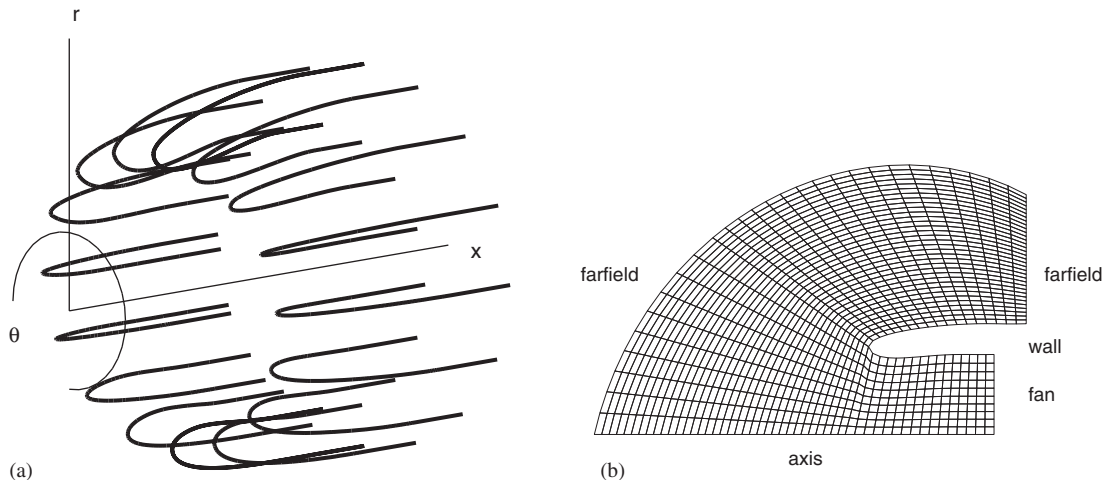

Fig. 2. 3D view of an asymmetric inlet geometry described by a series of axial sections at a number of equally spaced θ stations (a). Coarse quadrilateral mesh fitted around the axisymmetric mean of the same inlet (b).

and choosing a discretisation of the unit interval common for all the sections. Further, the axial and radial coordinates of these corresponding nodes in each section are discrete Fourier transformed in the θ direction. As a result of this process, the inlet is spectrally represented by a series of nodal coordinates which define the circumferential mean geometry of the inlet as well as by a series of corresponding nodal values of the modes giving the circumferential variation about that mean.

The next step is to construct a computational mesh for the given asymmetric inlet. First, a 2D mesh is build around the circumferential mean definition of the inlet geometry found in the manner described above, Fig. 2(b). The axial and radial coordinates of this mesh, respectively denoted x_0 and r_0, define the axisymmetric circumferential mean of the nodal coordinates of the final mesh. Then, the modes of asymmetry of the inlet geometry are interpolated on the 2D mesh from the pre-computed values at the inlet nodes to zero at the axis of symmetry and the farfield and fan boundaries. The result is a series of modes, denoted x_m and r_m, which describe the circumferential variation of the mesh nodal coordinates around the mean coordinates x_0 and r_0, respectively. At this point, the computational mesh is complete and its coordinate representation is a hybrid which combines the standard FE interpolation in the axial and radial coordinates (using the same shape functions N_n as in the axisymmetric case) with a Fourier series summation in the circumferential coordinate:

$$x(\xi,\eta,\theta) = \sum_m \sum_n x_{mn} N_n(\xi,\eta) \exp(im\theta),$$

$$r(\xi,\eta,\theta) = \sum_m \sum_n r_{mn} N_n(\xi,\eta) \exp(im\theta). \tag{27}$$

Such a mesh can be viewed as discrete in the axial and radial coordinates but continuous in the circumferential. Alternatively, any element from this mesh can be imagined as a torus whose circumferential variation is described by the coordinate modes; at an arbitrary θ station, the coordinates within the torus are given by Eq. (27).

In the above representation, the circumferential Fourier spectrum is finite, $-M \leqslant m \leqslant +M$, and, as inlet geometries are normally not far from symmetry, the number M of modes retained in the geometry representation is small. Moreover, as coordinates are real valued, corresponding "positive" and "negative" modes (e.g. x_{-m} and x_{+m}) form complex conjugate pairs.

Similar to the coordinates, the mean flow potential and acoustic potential fields are represented using the circumferential mean and the spectrum of circumferential variation. Thus, the field values are interpolated within each element using the double summation over element nodes and modal values:

$$\phi(\xi,\eta,\theta) = \sum_m \sum_n \phi_{mn} N_n(\xi,\eta) \exp(im\theta), \tag{28}$$

$$\hat{\phi}(\xi,\eta,\theta) = \sum_m \sum_n \hat{\phi}_{mn} N_n(\xi,\eta) \exp(im\theta + i\kappa\theta). \tag{29}$$

Obviously, unlike the coordinate modes x_{mn} and r_{mn} which are input to the analysis, the potential modes ϕ_{mn} and $\hat{\phi}_{mn}$ are the unknowns. Because the steady potential is real valued, the coefficients of corresponding modes in its circumferential spectrum form complex conjugate pairs but this property does not hold for the acoustic potential which is complex valued. Another difference is that, because the acoustic excitation at the fan is of known circumferential number κ, the spectrum of the acoustic potential is centred on mode κ rather than on 0 as is the case with the steady potential.

The Fourier spectrum involved in this representation is expected to be broader than for the inlet geometry, especially for the acoustic potential field which has a length scale of variation much smaller than the geometry. However, the number of modes required for an accurate spectral representation is not normally known a priori and should be found by trying different values in separate calculations; this issue will be exemplified later.

4.2. Gradient evaluation

In addition to steady and acoustic potential values, the discretisation requires the gradients of these fields which are obtained directly from the hybrid FE/spectral representation. For instance, from Eq. (28), the steady potential gradient is interpolated within each cell using the nodal values of the circumferential Fourier modes and the gradients of the interpolation functions:

$$\nabla\phi = \sum_m \sum_n \phi_{mn} \nabla(e^{im\theta} N_n).$$

Recalling the gradient in cylindrical coordinates is $\nabla = (\partial/\partial x, \partial/\partial r, r^{-1}\partial/\partial\theta)^T$ and denoting the gradient of the shape function in the (ξ, η) coordinates as $\nabla_\xi N_n = (\partial N_n/\partial\xi, \partial N_n/\partial\eta, 0)^T$, it can be shown that

$$\nabla(e^{im\theta} N_n) = e^{im\theta}(\mathbf{J}\mathbf{\Lambda})^{-1}(\nabla_\xi N_n + imN_n e_\theta). \tag{30}$$

This gradient identity involves the Jacobian $\mathbf{J} = \partial(x, r, \theta)/\partial(\xi, \eta, \theta)$, the matrix $\mathbf{\Lambda} = \text{diag}(1, 1, r)$ and the vector $e_\theta = (0, 0, 1)^T$.

Using bi-quadratic elements, the gradient has cross-element continuity in the axial and radial coordinates; continuity in the circumferential direction is ensured by the Fourier terms.

4.3. Weak formulation

The gradient identity enables one to evaluate the integrals in the weak formulations of the mean flow and acoustic problems in terms of 2D Gauss quadrature in (ξ, η). Indeed, introducing Eqs. (28) and (30) into the mean flow weak formulation (5) and using the test function $1/2\pi N_n \exp(-im\theta)$, the contribution from a particular node n to the volume integral is

$$\frac{1}{2\pi}\int_0^{2\pi}\int_0^1\int_0^1 e^{-im\theta}\rho\nabla\phi\cdot((\mathbf{J}\mathbf{\Lambda})^{-1}(\nabla_\xi N_n - imN_n e_\theta))|\mathbf{J}_0|r\,d\xi\,d\eta\,d\theta. \tag{31}$$

By integrating in space first, this can further be written in the following form, useful later:

$$\frac{1}{2\pi}\int_0^{2\pi} e^{-im\theta}[f(\theta) - img(\theta)]\,d\theta, \tag{32}$$

with

$$f(\theta) = \int_0^1\int_0^1 \rho\nabla\phi\cdot((\mathbf{J}\mathbf{\Lambda})^{-1}\nabla_\xi N_n)|\mathbf{J}_0|r\,d\xi\,d\eta, \tag{33}$$

$$g(\theta) = \int_0^1\int_0^1 \rho\nabla\phi\cdot((\mathbf{J}\mathbf{\Lambda})^{-1}N_n e_\theta)|\mathbf{J}_0|r\,d\xi\,d\eta. \tag{34}$$

The surface integral in Eq. (5) has a non-zero contribution from the fan face but, due to fan axisymmetry, this contribution is the same as in the axisymmetric case.

In a similar fashion, the modal representations (28) and (29) along with the test functions $1/2\pi N_n \exp(-i\kappa\theta - im\theta)$ are used to express the contribution to the volume integral in the acoustic weak formulation (6) at node n as

$$\frac{1}{2\pi}\int_0^{2\pi}\int_0^1\int_0^1 e^{-i(\kappa+m)\theta}\{(\rho\nabla\hat{\phi} + \hat{\rho}\nabla\phi)\cdot(\mathbf{J}\mathbf{\Lambda})^{-1}\cdot(\nabla_\xi N_n - i(\kappa+m)N_n e_\theta) - i\omega\hat{\rho}N_n\}|\mathbf{J}_0|r\,d\xi\,d\eta\,d\theta. \tag{35}$$

Similar to the steady residual case, integration in space leads to the following form of the above contribution:

$$\frac{1}{2\pi}\int_0^{2\pi} e^{-i(\kappa+m)\theta}[\hat{f}(\theta) - i(\kappa+m)\hat{g}(\theta)]\,d\theta, \tag{36}$$

in which the functions $\hat{f}$ and $\hat{g}$ are defined by

$$\hat{f}(\theta) = \int_0^1 \int_0^1 \{(\rho \nabla \hat{\phi} + \hat{\rho} \nabla \phi) \cdot (\mathbf{J\Lambda})^{-1} \cdot \nabla_\xi N_n - i\omega \hat{\rho} N_n\} |\mathbf{J}_0| r \, \mathrm{d}\xi \, \mathrm{d}\eta, \tag{37}$$

$$\hat{g}(\theta) = \int_0^1 \int_0^1 (\rho \nabla \hat{\phi} + \hat{\rho} \nabla \phi) \cdot (\mathbf{J\Lambda})^{-1} \cdot N_n \, e_\theta |\mathbf{J}_0| r \, \mathrm{d}\xi \, \mathrm{d}\eta. \tag{38}$$

Lastly, due to the axial symmetry of the fan face and far-field boundaries, the integral over these boundaries in Eq. (6) can be written as a sum of independent circumferential mode contributions, the contribution from each mode being described by the respective boundary condition of the axisymmetric discretisation with the corresponding circumferential wavenumber. However, the acoustic liner surface is not axisymmetric in general so the corresponding boundary integral couples the circumferential Fourier modes of the acoustic field and the integral has to be treated in a fashion similar to Eq. (35).

4.4. Discretisation

Grouping the steady potential values by circumferential Fourier mode within the vector $\mathbf{\Phi} = (\mathbf{\Phi}_{-M}, \ldots, \mathbf{\Phi}_0, \ldots, \mathbf{\Phi}_{+M})^{\mathrm{T}}$, with the individual modal vector $\mathbf{\Phi}_m$ containing the unknown nodal values ϕ_{mn} of the circumferential mode m, the mean flow potential problem is discretised as the system of nonlinear equations

$$\mathbf{r}(\mathbf{\Phi}) = 0. \tag{39}$$

The vector $\mathbf{r}$ of residual values has the same structure as $\mathbf{\Phi}$ and the residual value at node n in circumferential mode m is defined by Eq. (31), to which the fan boundary contribution is added if $m = 0$.

The discretisation of the acoustic problem in the weak formulation leads to a linear algebraic system which has the same structure as the discrete axisymmetric acoustic problem (18):

$$(\hat{\mathbf{L}} + \hat{\mathbf{F}})\hat{\mathbf{\Phi}} = \hat{\mathbf{f}}. \tag{40}$$

Similar to the discrete steady potential vector, the acoustic solution $\hat{\mathbf{\Phi}}$ has the modal representation $(\hat{\mathbf{\Phi}}_{-M}, \ldots, \hat{\mathbf{\Phi}}_0, \ldots, \hat{\mathbf{\Phi}}_{+M})^{\mathrm{T}}$, with the modal vector $\hat{\mathbf{\Phi}}_m$ containing the unknown nodal values $\hat{\phi}_{mn}$ of the circumferential mode m.

The discretisation of the volume integral in the weak formulation of the acoustic problem produces the matrix $\hat{\mathbf{L}}$. However, the matrix $\hat{\mathbf{L}}$ is notional and is not assembled explicitly because, as explained in the next section, only the residual $\hat{\mathbf{L}}\hat{\mathbf{\Phi}}$ is needed during the solution process.

The volume operator $\hat{\mathbf{L}}$ couples the circumferential modes in the acoustic solution $\hat{\mathbf{\Phi}}$; for instance, the solution mode $\hat{\mathbf{\Phi}}_0$ in the 3D solution is different from the axisymmetric acoustic field around the circumferential mean of the inlet geometry as it depends on the modes of asymmetry as well as on the axisymmetric mean.

On one hand, the discretisation of the surface integral in the acoustic weak formulation is simpler than that of the volume integral. This is due to the fact that the farfield and fan boundaries are axisymmetric; the farfield boundary can be freely chosen so in the mesh generation process while the fan geometry is necessarily circular. Consequently, the 3D farfield and fan boundary conditions are treated in exactly the same way as for axisymmetric geometries, i.e. applied independently to each circumferential mode of the acoustic potential field. Therefore, if no acoustic liner is present, the boundary operator $\hat{\mathbf{F}}$ is block diagonal, with each block $\hat{\mathbf{F}}_m$ defined by Eqs. (23) and (25) to represent the appropriate boundary condition for the circumferential mode number $m + \kappa$ in the acoustic solution. This involves the recalculation, for each circumferential mode, of the parameter λ in the far-field boundary condition and of the set of duct eigenmodes and axial wavenumbers in the fan boundary condition.

On the other hand, the boundary condition at the acoustic liner generally couples all the acoustic solution modes and the discretisation of the impedance condition surface integral (10) follows exactly the same steps as the discretisation of the volume integral. At the discrete level, therefore, the boundary condition at an non-axisymmetric acoustic liner configuration contributes off-diagonal block terms to the operator $\hat{\mathbf{F}}$. However, as

in the case of the matrix $\hat{\mathbf{L}}$, these are not formed explicitly and the residual contribution $\hat{\mathbf{F}}\hat{\boldsymbol{\Phi}}$ from the liner boundary condition is rather obtained from the spectral treatment of the boundary integral (10).

5. Solution process

Similar to its axisymmetric counterpart, the 3D mean flow problem (39) is solved using a Newton iteration with the update at step k defined by $\mathbf{K}\Delta\boldsymbol{\Phi}^{(k)} = -\mathbf{r}(\boldsymbol{\Phi}^{(k)})$. The off-diagonal blocks of the Jacobian matrix $\mathbf{K} = \partial\mathbf{r}/\partial\boldsymbol{\Phi}$ are non-zero, so the circumferential modes of the steady potential are coupled. Although $\mathbf{K}$ is sparse, a direct solution of this update is generally prohibitive as its cost is roughly proportional to $M^3 N^2$, where M is the number of solution modes and N the number of mesh nodes in the (x, r) coordinates. This cost comes from the fact that while $\mathbf{K}$ is a full matrix in modal space (non-zero off-diagonal blocks), it is sparse in the axial and radial coordinate space (each block is sparse). However, $\mathbf{K}$ is symmetric and positive definite and the Newton update equations can be efficiently solved using the conjugate gradient (CG) method [16]. Moreover, the equations can be preconditioned using an asymptotic approximation of $\mathbf{K}$ in the limit of axisymmetry whereby the non-axisymmetry of both the coordinates and the mean flow potential is neglected. With $\mathbf{K}_0$ and $\mathbf{K}_\theta$, respectively, defined by Eqs. (17) and (22), this preconditioner is the block diagonal matrix

$$\text{diag}(\mathbf{K}_0 + M^2\mathbf{K}_\theta, \mathbf{K}_0 + (M-1)^2\mathbf{K}_\theta, \ldots, \mathbf{K}_0, \ldots, \mathbf{K}_0 + (M-1)^2\mathbf{K}_\theta, \mathbf{K}_0 + M^2\mathbf{K}_\theta),$$

which depends only on the mean axisymmetric coordinates (x_0, r_0) and axisymmetric mean flow solution ϕ_0. Due to its block structure, preconditioning the Newton update is equivalent to a series of inexpensive direct 2D solutions, one for each circumferential mode of the solution.

Although the matrix $\hat{\mathbf{L}}$ is Hermitian, the boundary operator $\hat{\mathbf{F}}$ is not and the discrete acoustic problem (40) must be solved using an iterative solver appropriate for non-Hermitian systems. In this work, the quasi-minimal residual (QMR) [17] and the bi-conjugate gradient stabilised (BICGSTAB) [18] algorithms have been implemented. Both algorithms are related to the bi-conjugate gradient algorithm which iteratively constructs two mutually orthogonal sequences of residuals, one based on the system matrix and the other on its Hermitian [16]; however, only the QMR algorithm requires residuals like $(\hat{\mathbf{L}} + \hat{\mathbf{F}})^H \hat{\boldsymbol{\Phi}}$ while BICGSTAB is formulated using Hermitian free residuals.

Following the same approach as for the mean flow problem, the linear system (40) is preconditioned using the block diagonal matrix

$$\text{diag}(\hat{\mathbf{L}}_{-M} + \hat{\mathbf{F}}_{-M}, \hat{\mathbf{L}}_{-M+1} + \hat{\mathbf{F}}_{-M+1}, \ldots, \hat{\mathbf{L}}_0 + \hat{\mathbf{F}}_0, \ldots, \hat{\mathbf{L}}_{M-1} + \hat{\mathbf{F}}_{M-1}, \ \hat{\mathbf{L}}_M + \hat{\mathbf{F}}_M),$$

which represents an asymptotic approximation of the operator $\hat{\mathbf{L}} + \hat{\mathbf{F}}$ in the sense explained above, and depends on the axisymmetric mean modes of the geometry and mean flow. As with the mean flow problem, preconditioning Eq. (40) is equivalent to a series of 2D solutions due to the block diagonality.

The convergence of the QMR and BICGSTAB algorithms can, in theory, experience breakdown but, using the above preconditioner, both performed very well on all the 3D problems solved throughout this research. Another obvious candidate for a linear solver would be the popular generalised minimal residual (GMRES) algorithm [19] but QMR and BICGSTAB are computationally much cheaper and, so far, there has been no need to implement the more robust GMRES. However, if implemented, GMRES would benefit from the same preconditioner.

6. Residual evaluation

The iterative solution methods CG, QMR and BICGSTAB require the ability to compute products of the system matrices $\mathbf{K}$ and $\hat{\mathbf{L}} + \hat{\mathbf{F}}$ and arbitrary vectors $\boldsymbol{\Phi}$ and $\hat{\boldsymbol{\Phi}}$, respectively. As mentioned earlier, these matrices are not available because of large memory storage requirements but the matrix–vector products are instead computed directly as discretisations of the weak formulations. This computation involves a transformation from the modal Fourier domain of the vectors $\boldsymbol{\Phi}$ and $\hat{\boldsymbol{\Phi}}$ to the domain of θ dependence as well as the transformation back to the modal representation of the residual.

For instance, the matrix–vector product $\hat{\mathbf{L}}\hat{\boldsymbol{\Phi}}$ is computed from the volume integral definition (35) as follows. First, for each Gauss quadrature point of coordinates (ξ, η), the circumferential modes of both the coordinates

and potential field are interpolated from the nodal values using the shape functions N_n. This process corresponds to the summation over nodes n in the hybrid FE/spectral representation. Then, at the same Gauss point, the coordinates x, r and the potential values ϕ, $\hat{\phi}$ are computed along with their gradients with respect to (x, r, θ) at a number M_θ of "virtual" equally spaced points in the circumferential direction. This process is achieved by applying the inverse fast Fourier transform (FFT) algorithm [12,20] to the respective circumferential modal values at (ξ, η), which corresponds to the summation over modes m in the FE/spectral representation. (To minimise aliasing errors while maintaining a low computational cost, M_θ is the smallest power of 2 which is larger than four times the largest Fourier mode number in the coordinate and potential modal representation.) Then, using the values of the coordinates, potential and gradients, the values of the functions $\hat{f}$ and $\hat{g}$ defined by Eqs. (37) and (38) are computed at the "virtual" circumferential points, with the (ξ, η) integration achieved through Gauss quadrature. Lastly, the volume integral is completed in θ by applying the direct FFT to the "virtual" point values of $\hat{f}$ and $\hat{g}$. The modal values $\hat{f}_m$ and $\hat{g}_m$ computed in this manner are then combined to obtain the matrix–vector product in the spectral representation as $\hat{f}_m - \mathrm{i}(\kappa + m)\hat{g}_m$. The mean flow residual $\mathbf{r}(\boldsymbol{\Phi})$ as defined by Eq. (31) is computed in exactly the same manner.

The same procedure is also followed to evaluate the impedance condition contribution $\hat{\mathbf{F}}\hat{\boldsymbol{\Phi}}$ to the discrete residual of the acoustic equation as defined by Eq. (10). The Fourier circumferential modes of $\hat{\boldsymbol{\Phi}}$ are coupled by this boundary condition in the case of an asymmetric liner geometry and the surface integral contribution is obtained in a way similar to the volume integral. However, a slight variation of this procedure is adopted in the case of acoustic liners with circumferential non-uniformity (e.g. spliced liners). In that case, the impedance value Z is a function of θ which could be specified at a number of non-uniformly spaced circumferential locations and/or could vary non-continuously. The FFT algorithm and its inverse must then be replaced by a computationally slower implementation of the discrete Fourier transform on non-uniformly spaced points.

Unlike the liner case, the boundary condition contributions from farfield and fan face are computed directly in the spectral representation as the circumferential modes are not coupled by the respective conditions; the contribution to residual mode m is simply $\hat{\mathbf{F}}_m\hat{\boldsymbol{\Phi}}_m$.

Finally, the Newton update residual $\mathbf{K}\boldsymbol{\Phi}$ is in fact the matrix–vector product $\hat{\mathbf{L}}\boldsymbol{\Phi}$ computed for zero values of the frequency ω and circumferential mode number κ. Also, the residual $(\hat{\mathbf{L}} + \hat{\mathbf{F}})^H \hat{\boldsymbol{\Phi}}$ of the acoustic matrix Hermitian required by QMR can be obtained easily as the operator $\hat{\mathbf{L}}$ is self-adjoint and the boundary contributions are straightforward to modify for the adjoint residual.
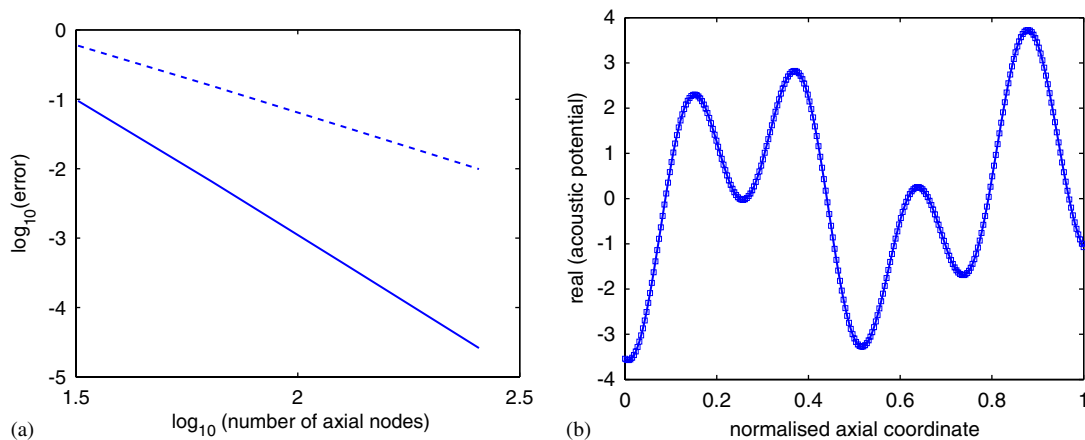

Fig. 3. Convergence of the computed acoustic field within an infinite hard-walled duct to the analytic solution (a): the variation of error (rms of difference between computed and analytic solution) with the axial discretisation is second order for bi-linear FE (– –) and fourth for bi-quadratic (—). The acoustic field within a blocked semi-infinite hard-walled duct is a superposition of the incident and reflected waves (b): the computed solution (—) is in very good agreement with the analytic (□).

7. Method validation

The new hybrid spectral/FE method was validated on a number of testcases; the first part of these tests was concerned with the accuracy of the axisymmetric analysis and the second part with the ability of the spectral method to predict correctly 3D features of the acoustic field.

Most of the axisymmetric testcases have analytic solutions against which the corresponding numerical solutions were directly compared. The first such testcase consists of an infinite hard-walled cylindrical duct with uniform flow along which a cut-on duct eigenmode propagates. Retaining a finite length of the duct in the numerical calculation, a FE convergence test proves the numerical solution converges to the analytic in the limit of a fine mesh, Fig. 3(a). The second testcase is a semi-infinite hard-walled cylindrical duct with uniform flow and a perfectly reflective hard-wall termination; a cut-on eigenmode is incident at the free end. Although physically unrealistic, this testcase is useful to verify the correct treatment of the reflected duct eigenmode, Fig. 3(b), and to test the non-reflective boundary condition at the duct free end. The third case is a test for the non-reflectivity of the boundary condition at the farfield and consists of a hard-walled sphere which vibrates or pulsates harmonically in stagnant gas. Using a rectangular computation domain to force the acoustic waves across the far-field boundary at an angle, the computed and analytic solutions are in very good agreement at a moderately high frequency, Fig. 4.

The last axisymmetric test compares the solution obtained using the new spectral method with the result from the proprietary aeroacoustics software ACTRAN [21], which has the same impedance acoustic liner condition as well as the fan modal boundary condition. Two geometries were considered, the first a cylindrical duct and the second the annular aft duct of a modern high-bypass turbofan, Fig. 5. Both ducts contained mean flow and had axisymmetric acoustic liners of circumferentially uniform impedance. In both cases, the new method used nine-node bi-quadratic quadrilateral elements while ACTRAN used eight-node serendipity
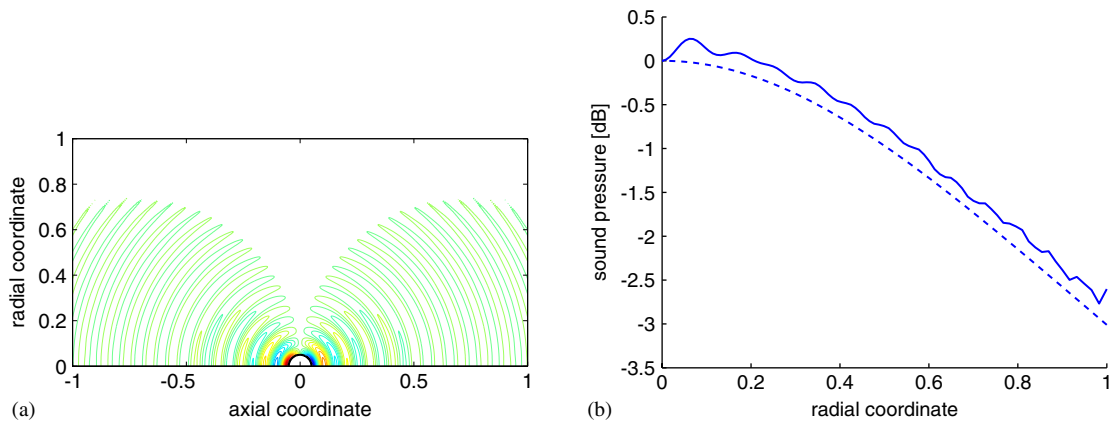

Fig. 4. Contours of the acoustic pressure generated by the horizontal harmonic vibration of a hard-walled sphere in stagnant gas, computed on a rectangular domain (a): the reduced frequency (based on the sphere radius) is 10π. Variation of the SPL along the l.h.s. far-field edge of the domain relative to the value on the axis of vibration (b): the computed (—) and analytic (– –) variations are in good agreement (within 0.3 dB) as reflections from the farfield into the domain are minimised by the far-field boundary condition.
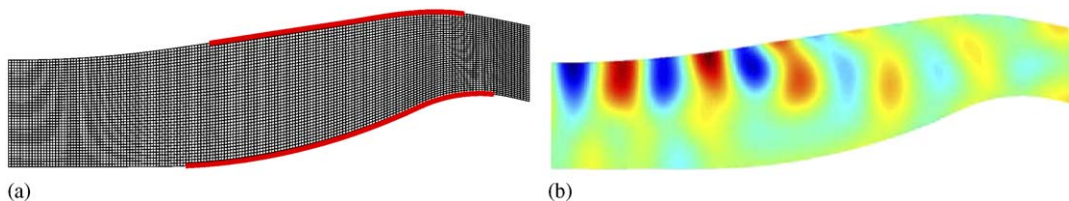

Fig. 5. Coarse mesh discretisation of the aft-duct of a high-bypass turbofan: (a) showing the location of the acoustic liners in thick lines. The acoustic pressure solution (b) excited by the duct eigenmode of radial order 0 incident at the fan outlet guide vane on the left.

Table 1

Table of errors (measured in %) of the transmitted intensity values in radial modes 0, 1 and 2 output by the new method relative to the corresponding values from ACTRAN. The duct eigenmodes of radial order 0, 1 and 2 were in turn incident at the fan boundary; because of the acoustic lining, each input radial mode also energises all other radial modes inside the duct

Transmitted	Incident		
	0	1	2
0	0.86	0.41	1.27
1	3.72	4.23	6.07
2	0.61	0.14	1.60
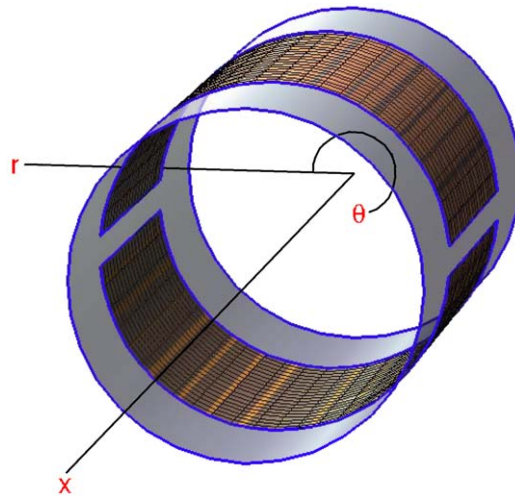
Fig. 6. Sketch of a cylindrical duct with a spliced acoustic liner. The liner is represented in a darker shade and the axes of cylindrical coordinates are also shown.

quadrilaterals but, apart from the element mid nodes, the computational meshes used by the two codes were the same. Also, the mean flow fields used by both the spectral method and ACTRAN were identical at the common mesh nodes while the new code used the mean value of the neighbouring nodes at each element mid node. Keeping the frequency fixed at 1.6 kHz and the circumferential mode number at 20, the duct eigenmodes of radial orders 0, 1 and 2 were in turn input at the inflow boundary of both the cylindrical duct and the engine aft duct. The validation was based on the sound intensities transmitted across the outflow boundary; the intensity value is the surface integral over the boundary of the local acoustic intensity [22] defined for each radial mode. The intensity values in the modes of radial order 0, 1 and 2 were computed independently using both the new code and ACTRAN; the values proved to be in very good agreement and they were no more than 3% off each other in the case of the cylindrical duct and 6% in the case of the aft duct, Table 1.

   The last validation test was concerned with the 3D effects of acoustic liner non-uniformity on the acoustic field inside an infinite cylindrical duct containing uniform flow. The validation case as well as the numerical data (obtained using ACTRAN) were taken from Ref. [23]. The geometry was a cylinder of radius 1.27 m with an acoustic liner extending longitudinally for 0.61 m. The liner had a constant impedance everywhere (non-dimensional value $2 - i$) except along two diametrically opposed hard wall thin splices (of infinite impedance), each extending circumferentially over an angle of $3.44°$. A sketch of the spliced liner geometry is given in Fig. 6; this mimics the presence of splices inside a real engine inlet due to the impossibility of manufacturing a continuous acoustic liner surface. Two cases were considered, one with zero flow and the other with a uniform flow of Mach number 0.4. In both cases, the duct eigenmode (0, 26) was incident at the outflow; the first number indicates the radial order and the second the circumferential mode number. Keeping the cut-on ratio
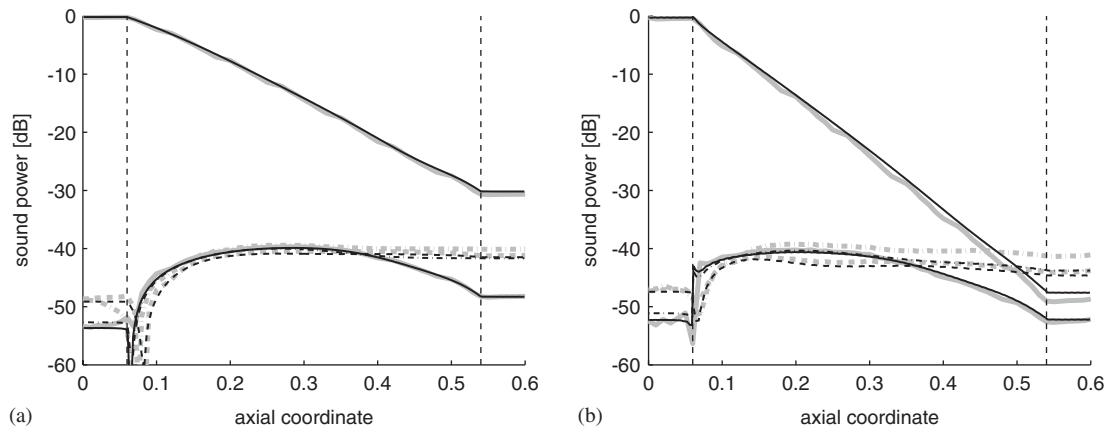
Fig. 7. Axial variation of the SPL along a cylindrical duct with a spliced acoustic liner: the no-flow case (a) and the Mach number 0.4 case (b). The values obtained using the new method are shown in thin black lines while those from ACTRAN are in thick grey lines. The SPL of the incident circumferential mode $m = 26$ is represented in continuous line and starts close to 0 dB. Other modes depicted are 24 (—), 22 (– –) and 20 (· – ·). The axial positions of the acoustic liner limits are marked in vertical dashed lines; the sound power absorption due to the liner is thus clear in the incident mode.

constant at 1.1, the reduced frequency (based on the duct radius) was 24.61 in the zero flow case and 22.56 in the other. The new method used a mesh with 133 by 41 nodes in the respective axial and radial directions (ensuring more than 50 nodes per wavelength) and required $2M + 1 = 53$ Fourier modes for a good circumferential resolution.

Figs. 7(a) and (b) depict the variation of the sound power level (SPL) along the duct, comparing the values predicted by the spectral method with those from ACTRAN. At each axial station, the SPL is computed using the sound intensity which is, this time defined as the duct cross-section integral of the local acoustic intensity defined for each circumferential mode number. By analogy with rotor–stator interaction, due to the presence of the splices, the incident mode $\kappa = 26$ is scattered into the modes of circumferential numbers given by the sequence $\kappa \pm js$ with $s = 2$ the number of splices and j an arbitrary integer. Figs. 7(a) and (b) indicate a good agreement between the results from the new method and those from the commercial code; although only a few circumferential modes ($j = 0, -1, -2, -3$) modes are shown for an easy visual inspection, the comparison is equally good for all other excited modes. The small differences between the two sets of results are partly due to the fact that the acoustic fields were computed on different meshes by the two codes as well as to the differences in post-processing in order to obtain the SPL values.

8. Numerical results

A further set of results obtained on a realistic geometry illustrate the use of the new spectral method in practical terms. These results concern the calculation of the acoustic field of a single high frequency and circumferential mode number propagated forward of a real engine inlet without acoustic liner treatment.

The engine inlet geometry was asymmetric with a scarfing angle of about $5°$ (the angle between the plane of the inlet front and the engine axis) and could be accurately described using the axisymmetric mean and four circumferential Fourier modes of asymmetry, i.e. using the modes $-2 \leqslant m \leqslant +2$. The mean flow had a Mach number of 0.3 at the freestream and which became accelerated to 0.4 at the fan. Considering the first blade passing frequency excitation and 26 fan blades, the incident circumferential mode number was $\kappa = 26$ and the reduced frequency (based on engine radius and freestream speed of sound) 30. Then, only the first radial order mode was cut-on at the fan boundary. The computational mesh used bi-quadratic elements and 14,000 nodes in the axial and radial directions, ensuring a minimum of eight nodes per wavelength.

Although four circumferential Fourier modes were enough to describe the asymmetric inlet geometry, the number of modes required to accurately represent the acoustic field was expected to be greater, as the acoustic field with a high circumferential wavenumber is less smooth than the geometry. In order to determine this
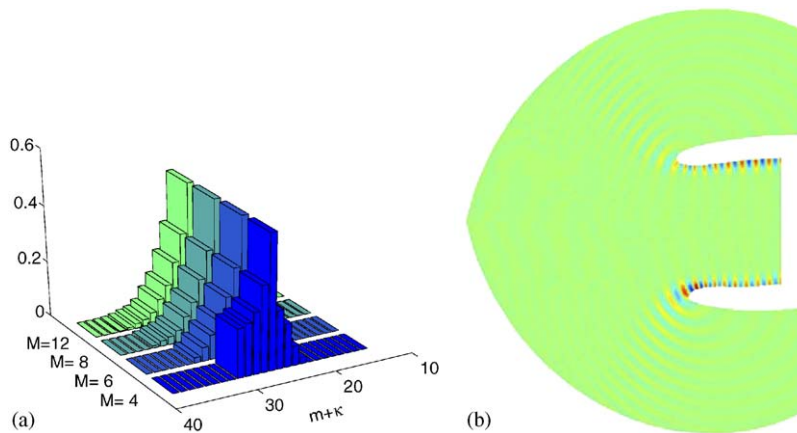
Fig. 8. The variation of the "energy" distribution across circumferential mode number $m + \kappa$ with the number M of circumferential modes used to represent the acoustic solution (a); there is no practical difference between the distribution at $M = 8$ and 12. An axial section depiction of the acoustic pressure solution obtained using $M = 8$ (b).
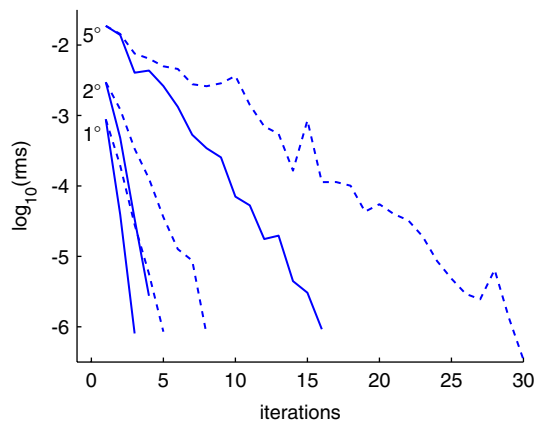

Fig. 9. Convergence histories of the BICGSTAB (—) and QMR (– –) spectral iterative methods for the inlet configurations with $1°$, $2°$ and $5°$ scarfing. The lower the degree of asymmetry, the more efficient the preconditioner is and the faster the convergence.

number, a convergence test was performed through a series of calculations in which Fourier modes were added until the acoustic solution converged. Thus, four separate calculations used $M = 4, 6, 8$ and 12 modes and convergence was monitored using the distribution of "energy" (the RMS of the solution vector in each mode) across the Fourier modes, Fig. 8(a). The modal "energy" distribution in the case $M = 12$ did not change significantly relative to the case $M = 8$ (using modes $-8 \leqslant m \leqslant +8$), therefore, the latter was practically sufficient to obtain the solution with satisfying accuracy. Fig. 8(b) is a vertical axial section through the acoustic pressure solution obtained using $M = 8$ and depicts clearly the asymmetry of both the geometry and of the computed acoustic field.

To illustrate the convergence properties of the spectral iterative solver based on the QMR and BICGSTAB algorithms, a series of calculations was performed with different degrees of asymmetry. Thus, keeping the axisymmetric circumferential mean of the same engine inlet geometry as above but linearly scaling all the modes of asymmetry, configurations with scarfing angles of $1°$ (almost axisymmetric), $2°$ and $5°$ (original geometry) were obtained. For each of these configurations, a separate acoustic calculation was performed using the same parameters as for the inlet acoustic problem discussed above. Fig. 9 depicts the QMR and BICGSTAB convergence histories in these three cases and shows clearly how the convergence rate was greatest when the deviation from axisymmetry was smallest. This is explained by the fact that the
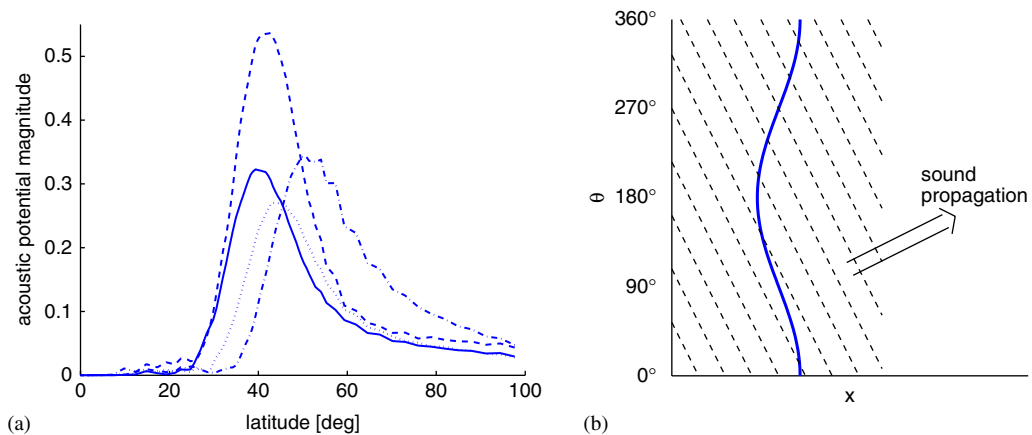
Fig. 10. Variation of the magnitude of the far-field boundary acoustic solution with the latitude angle at four different circumferential locations (a); — for $\theta = 0°$, – – for $90°$, · – · for $180°$ and · · · for $270°$. Sketch of the engine inlet surface unwrapped in the circumferential angle coordinate (b); the fan is on the left and the farfield on the right.

preconditioner, based on an asymptotic axisymmetric approximation, is most effective when the degree of asymmetry is smallest.

Lastly, an interesting aspect of these results is the "left–right" asymmetry of the acoustic field radiated towards the farfield. Indeed, although the inlet geometry is symmetric with respect to the vertical axial plane, the acoustic solution is not. Fig. 10(a) depicts the variation of the magnitude of the far-field boundary acoustic solution $\hat{\phi}$ (reconstructed from the circumferential Fourier representation) with the latitude angle (measured from the engine axis at the inlet plane location). This variation is shown at four different circumferential locations: $\theta = 0°$ (engine top), $\theta = 90°$ (right side as looking at engine from front), $\theta = 180°$ (engine bottom) and $\theta = 270°$ (left side). While this variation has roughly the same form at different circumferential locations, it peaks at a different maximum indicating a strong asymmetry. Thus, the maximum value of $|\hat{\phi}|$ at $\theta = 0°$ is slightly smaller than at $\theta = 180°$ and this is to be expected as the positive scarfing of the inlet directs noise towards the ground. However, the maximum at $\theta = 90°$ is roughly double the same value at $\theta = 270°$ and bigger than at $\theta = 180°$; this results in a "left–right" difference of about 6 dB in noise intensity. Of course, the variation discussed here is at the numerical far-field boundary rather than at the physical farfield, nevertheless the observations are expected to be correct also at the latter.

This asymmetric radiation pattern can be explained using ray theory on Fig. 10(b) which shows a sketch of the engine inlet surface unwrapped in the circumferential angle coordinate θ. Sound travels from the fan (left) towards the inlet highlight (right) at an acute angle with the fan plane because of the high circumferential mode number. Also, because of the positive scarfing, the inlet highlight (thick solid line) extends forward of the fan to a greater extent at the top ($\theta = 0°$ and $360°$) than at the bottom ($\theta = 180°$). Consequently, at different circumferential locations, the crests of the sound perturbation (thin dashed lines) cross the highlight at different angles. This angle determines the strength of the sound radiated towards the farfield; the maximum strength is roughly at $\theta = 90°$ where the angle between the direction of propagation and the highlight line is maximum.

Ref. [2] reports comparable results in which the acoustic field inside a plane-symmetric helicopter engine inlet duct deviates from the plane-symmetry of the inlet geometry as the non-zero spinning modes interact with the geometric variation about axial symmetry.

9. Performance aspects

The new spectral aeroacoustic method has two important advantages over a standard 3D FE approach: it requires significantly fewer unknowns and it benefits from an efficient specialised preconditioner.

First, consider the engine inlet problem discussed above. With 14,000 nodes in the computational mesh and $2M + 1 = 17$ circumferential Fourier modes in the solution, the total number of unknowns was 0.24 million.

The equivalent acoustic calculation using a standard 3D FE formulation with a minimum of eight nodes per wavelength in the circumferential direction and using the same axial and radial resolution requires approximately 3 million unknowns. Even for the spliced acoustic liner problem used for validation, where the number of circumferential Fourier modes used was higher ($2M + 1 = 53$), the equivalent standard FE approach must use at least eight times the highest cut-on circumferential wavenumber (28) resulting in a total number of unknowns more than four times greater than the spectral method.

Second, the specialised preconditioning strategy impacts on the method in two ways. On one hand, it ensures the solver iterations on the linear acoustic problem are stable even for larger degrees of asymmetry, allowing the use of a relatively inexpensive solution method, such as BIGCSTAB, in preference to the more general GMRES. On the other hand, the preconditioned iteration has a very good convergence rate; the acoustic solution for the $5°$ scarfing inlet was obtained with reasonable accuracy in about 15 iterations using BICGSTAB.

Lastly, it is worth also considering a couple of more practical performance aspects. First, the computer implementation of the new spectral method was carried out in Matlab. Programming benefited substantially from the high-level description of operations in Matlab as well as from a relative ease of code debugging. For instance, preconditioning is carried out using the Matlab sparse direct solver on each pre-computed diagonal block of the preconditioner. The second aspect is computing cost; the iterative solution of the linear acoustic system for the engine inlet application with $5°$ scarfing angle required about 3 h wall-clock time on a 3 GHz Pentium 4 PC using the BICGSTAB algorithm. This performance is comfortable even for such an application as the design optimisation of the inlet geometry where the calculation might be repeated for a large number of design configurations. Moreover, implementation of the new method in a programming language suitable for scientific computation, e.g. Fortran, should result in a significant speed-up in terms of wall-clock time, primarily due to a more efficient handling of nested loops in the residual calculation, which is inherently slow in Matlab.

10. Conclusions

This paper has introduced a novel method for the analysis of tone noise radiation from non-axisymmetric turbofan inlets with acoustic liner treatment. The method combines a standard FE discretisation of the acoustic field in the axial and radial coordinates with a Fourier spectral representation in the circumferential direction. The method requires much fewer unknowns than a standard 3D FE solution and is therefore computationally significantly less expensive. Moreover, the use of iterative linear solvers in conjunction with an efficient specialised preconditioning technique makes the new method very attractive for inlet aeroacoustic applications.

Numerical examples of practical relevance have demonstrated the prediction capabilities of the new method, with particular emphasis on acoustic liner modelling. An important aspect discussed was the number of Fourier modes retained in the acoustic solution for an accurate representation. Also, of great practical interest was the effectiveness of the preconditioner, illustrated clearly on a series of calculations with varying degrees of asymmetry.

Although the proposed method is particularly targeting the niche application of engine inlet aeroacoustics, it can be employed without modification in any situation where the degree of axial asymmetry is relatively low. In any such case, a relatively small number of circumferential Fourier modes is adequate for an accurate field representation. The method is also suited to cope with boundary conditions involving circumferentially varying or even discontinuous parameters, such as spliced acoustic liners.

References

[1] Y. Özyörük, L.N. Long, Computation of sound radiating from engine inlets, *AIAA Journal* 34 (5) (1996) 894–901.

[2] D. Stanescu, D. Ait-Ali-Yahia, W.G. Habashi, M.B. Robichaud, Multidomain spectral computation of sound radiation from ducted fans, *AIAA Journal* 37 (3) (1999) 296–302.

[3] Y. Özyörük, Parallel computation of forward radiated noise of ducted fans with acoustic treatment, *AIAA Journal* 40 (3) (2002) 450–455.

[4] L. Sbardella, B.J. Tester, M. Imregun, A time-domain method for the prediction of sound attenuation in lined ducts, *Journal of Sound and Vibration* 239 (3) (2001) 379–396.

[5] A. McAlpine, M.J. Fisher, On the prediction of ''buzz-saw'' noise in acoustically lined aero-engine inlet ducts, *Journal of Sound and Vibration* 265 (2003) 175–200.

[6] Y. Özyörük, E. Alpman, V. Ahuja, L.N. Long, Frequency-domain prediction of turbofan noise radiation, *Journal of Sound and Vibration* 270 (4–5) (2004) 933–950.

[7] R.J. Astley, W. Eversman, Wave envelope and finite element schemes for fan noise radiation from turbofan inlets, *AIAA Paper*, 83-0709, 1983.

[8] W. Eversman, A.V. Parrett, J.S. Preisser, R.J. Silcox, Contributions to the finite element solution of the fan noise radiation problem, *Transactions of the ASME* 107 (1985) 216–223.

[9] A.A. Rangwalla, M.M. Rai, A numerical analysis of tonal acoustics in rotor–stator interactions, *Journal of Fluids and Structures* 7 (1993) 611–637.

[10] C.L. Rumsey, R.T. Biedron, F. Farassat, P.L. Spence, Ducted-fan engine acoustic predictions using a Navier–Stokes code, *Journal of Sound and Vibration* 213 (4) (1998) 643–664.

[11] B. Fornberg, *A Practical Guide to Pseudospectral Methods*, Cambridge Monographs on Applied and Computational Mathematics, Cambridge University Press, Cambridge, 1996.

[12] L.N. Trefethen, *Spectral Methods in MATLAB*, SIAM, Philadelphia, 2000.

[13] W. Eversman, The boundary condition at an impedance wall in a nun-uniform duct with potential mean flow, *Journal of Sound and Vibration* 246 (1) (2001) 63–69.

[14] M.K. Myers, On the acoustic boundary conditions in the presence of flow, *Journal of Sound and Vibration* 71 (1980) 429–434.

[15] B. Regan, J. Eaton, Modelling the influence of acoustic liner non-uniformities on duct modes, *Journal of Sound and Vibration* 219 (5) (1999) 859–879.

[16] R. Barrett, M. Berry, T.F. Chan, et al., *Templates for the Solution of Linear Systems: Building Blocks for Iterative Methods*, SIAM, Philadelphia, PA, 1994.

[17] R.W. Freund, N.M. Nachtingal, QMR—a quasi-minimal residual method for non-Hermitian linear systems, *Numerische Mathematik* 60 (3) (1991) 315–339.

[18] H.A. van der Vorst, Bi-CGSTAB: a fast and smoothly converging variant of Bi-CG for the solution of non-symmetric linear systems, *SIAM Journal on Scientific Computing* 13 (1992) 631–644.

[19] Y. Saad, GMRES: a generalized minimal residual algorithm for solving nonsymmetric linear systems, *SIAM Journal on Scientific and Statistical Computing* 7 (3) (1986) 856–869.

[20] FFTW software package, ⟨http://www.fftw.org/⟩, 2003.

[21] *MSC Actran 2003 User's Guide*, Free Field Technologies, 16 Place de l'Université, B-1348 Louvain-la-Neuve, Belgium, ⟨http://www.fft.be/⟩.

[22] M.E. Goldstein, *Aeroacoustics*, McGraw Hill Inc., New York, 1976.

[23] B.J. Tester, N.J. Baker, A.J. Kempton, M.C. Wright, Validation of an analytical model for scattering by intake liner splices. *AIAA Paper* AIAA-20040-2906, *presented at the 10th AIAA/CEAS Aeroacoustics Conference*, Manchester, UK, 10–12 May 2004.